EPJ Web of Conferences **364**, 01013 (2026) https://doi.org/10.1051/epjconf/202636401013
Quark Matter 2025

Experiment highlights on chiral magnetic effects, spin polarization, and spin alignment

Zhiwan Xu[1,*]

[1]Argonne National Laboratory, Lemont, IL 60439, USA

Abstract. High-energy heavy-ion collisions produce quark–gluon matter in strong rotation and immersed in short-lived, intense magnetic fields. These unique conditions enable studies of novel quantum chromodynamics phenomena, including chiral magnetic effects, global spin polarization, and spin alignment. Measurements in small systems also provide access to longitudinal polarization and local spin correlations. We review recent highlights from experiments at RHIC and the LHC, including the results on the chiral effects, intriguing hyperon global polarization, spin alignment, and local spin correlations.

1 Introduction

Relativistic nuclear collisions at RHIC and the LHC create the quark–gluon plasma (QGP), the most vortical fluid, where quarks and gluons are deconfined at temperatures $T > \Lambda_{\rm QCD}$. In noncentral collisions, the large initial orbital angular momentum ($L \sim 10^3$–$10^5\ \hbar$) induces global rotation and strong local vorticity [1], while the positively charged nuclei generate extremely strong, short-lived magnetic fields ($B \sim 10^{13}$–10^{15} T) [2]. These conditions enable studies of nuclear matter under intense vorticity and electromagnetic fields.

In the presence of a chirality imbalance, the magnetic field can couple to quark spins and induce charge separation phenomena such as the chiral magnetic effect (CME) and the chiral magnetic wave (CMW) [3, 4], probing the topological structure of the QCD vacuum. These chiral effects are expected to occur in the early stages of the QGP, but their experimental detection remains challenging due to flow-related backgrounds. The rotational field can also couple to quark spins, inducing global polarization of fermions ($J = 1/2,\ 3/2$) and spin alignment of vector mesons ($J = 1$). These spin-based observables provide complementary probes of mean-field strength, vorticity, electromagnetic effects, and QCD field fluctuations. In addition, small systems like p+p and p+Pb collisions provide unique insights into local vorticity and spin phenomena, including spin correlations and longitudinal hyperon polarization.

2 Chiral Effects

The charge separation from the CME is measured using two-particle correlations with respect to the reaction plane (Ψ) . Among multiple complementary observables [5–7], the most widely used is $\Delta\gamma^{112} = \gamma^{112}_{\rm OS} - \gamma^{112}_{\rm SS}$, where $\gamma^{112} = \langle\cos(\varphi_1 + \varphi_2 - 2\Psi)\rangle$. The dominant background originates from elliptic flow coupled with local charge conservation, transverse

*e-mail: zhiwan.xu@anl.gov

© The Authors, published by EDP Sciences. This is an open access article distributed under the terms of the Creative Commons Attribution License 4.0 (https://creativecommons.org/licenses/by/4.0/).

momentum conservation, and resonance decays. Additional nonflow backgrounds, unrelated to the reaction plane, also contribute, e.g., from di-jets. Isobar collisions (Ru+Ru and Zr+Zr) were employed to disentangle signal and background contributions, but no predefined CME signal was observed in their difference, and the interpretation was further hindered by uncertainties arising from multiplicity mismatches [8].

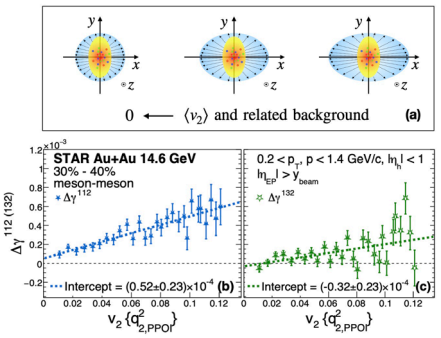

Figure 1. (a) Different particle emission patterns from the same initial geometry. (b) $\Delta\gamma^{112}$ and (c) $\Delta\gamma^{132}$ vs. v_2 in 30–40% Au+Au categorized with $q^2_{2,\mathrm{PPOI}}$ at $\sqrt{s_{NN}}$ = 14.6 GeV [12].

To reduce flow-related backgrounds, event-shape methods were first applied in LHC measurements [9, 10], though large uncertainties arise from long extrapolations to the zero-v_2 limit. A recently proposed event-shape selection (ESS) [11] captures local emission-pattern fluctuations and improves these extrapolations, as demonstrated in Au+Au collisions at $\sqrt{s_{NN}}$ = 14.6 GeV (Fig. 1) [12, 13]. Background reduction was validated using the observable $\Delta\gamma^{132} = \gamma^{132}_{\mathrm{OS}} - \gamma^{132}_{\mathrm{SS}}$, where $\gamma^{132} = \langle\cos(\varphi_1 - 3\varphi_2 + 2\Psi)\rangle$, and the unbiased signal was extracted from the intercept [14]. Measurements of $\Delta\gamma^{112(132)}$ employed low-momentum mesons relative to spectator planes from the event plane detector (EPD), enhancing alignment with the magnetic field direction and suppressing nonflow effects.

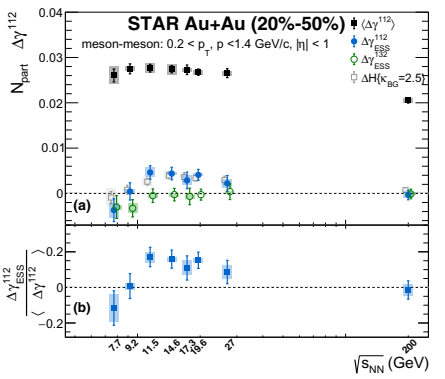

Figure 2. (a) Beam energy dependence of $N_{\mathrm{part}}\langle\Delta\gamma^{112}\rangle$, $N_{\mathrm{part}}\Delta\gamma^{112,132}_{\mathrm{ESS}}$, and $N_{\mathrm{part}}\Delta H(\kappa_{bg} = 2.5)$ in 20%–50% Au+Au as functions of beam energy. (b) Ratio $\Delta\gamma^{112}_{\mathrm{ESS}}/\langle\Delta\gamma^{112}\rangle$ [12].

STAR reported CME results from BES-II and top RHIC energies in Fig. 2 [12, 13]. $\Delta\gamma^{132}_{\mathrm{ESS}}$ is consistent with zero, confirming effective background removal. A finite charge separation signal in $\Delta\gamma^{112}_{\mathrm{ESS}}$ is observed at 11.5, 14.6, and 19.6 GeV with around $\sim 3\sigma$ significance each, combining to over 5σ. $\Delta\gamma^{112}_{\mathrm{ESS}}$ agrees with the BES-I $\Delta H \equiv H_{\mathrm{SS}} - H_{\mathrm{OS}}$ correlator [15], with $H(\kappa_{\mathrm{BG}}) \equiv (\kappa_{\mathrm{BG}}v_2\delta - \gamma^{112})/(1 + \kappa_{\mathrm{BG}}v_2)$ at $\kappa_{\mathrm{BG}} = 2.5$. The ratio $\Delta\gamma^{112}_{\mathrm{ESS}}/\langle\Delta\gamma^{112}\rangle$ shows that at least 80% of $\langle\Delta\gamma^{112}\rangle$ comes from background. The rise-and-fall beam-energy dependence that finite charge separation emerges between 10–20 GeV and vanishes below 10 GeV and at 200 GeV may reflect the interplay of magnetic field lifetime, topological vacuum transitions, and QGP duration, motivating further theoretical study.

ALICE reported particle-specific analyses to disentangle different background sources and provide additional constraints on the upper limit of the CME. The disappearance of the charge separation signal at top RHIC and LHC energies suggests a rapid decay of the magnetic field.

The CMW, which arises from the coupling of the CME and the chiral separation effect, produces an electric quadrupole and is quantified by r_2, the slope of $(v_2^- - v_2^+)$ versus charge asymmetry A_{ch}. STAR BES-II measurements show no enhancement of r_2 relative to the spectator plane compared with the participant plane. In isobar collisions, Ru+Ru and Zr+Zr comparisons are consistent with each other. These observations constrain the magnetic-field–driven effects and indicate significant background contributions.

3 Spin Polarization

Hyperon global polarization (P_H), induced by the system's orbital angular momentum, probes the QGP's vortical structure [16]. It is measured via the self-analyzing weak decay of hyperons: $P_H = \frac{8}{\pi\alpha_H}\frac{1}{A_0}\frac{\langle\sin(\Psi-\varphi^\star)\rangle}{Res(\Psi)}$, where $\varphi^\star$ is the daughter baryon's azimuthal angle in the parent's rest frame. STAR observed significant global polarization in Au+Au collisions at lower RHIC energies, corresponding to a large QGP vorticity $\omega \sim 10^{22}$ s^{-1} [17]. Recent BES-II measurements confirmed the increase of $\langle P_H\rangle$ for Λ hyperons toward lower energies with improved statistics (Fig. 3(a)), directly probing strange quark polarization. Theoretical calculations predict polarization saturation near 3 GeV, underscoring the importance of high-statistics measurements below 10 GeV [18, 19].

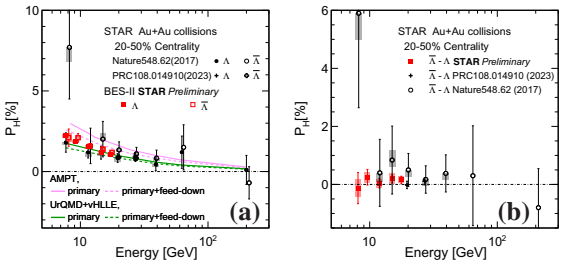

Figure 3. Beam energy dependence of (a) P_H of Λ and $\bar{\Lambda}$; (b) P_H difference between them in Au+Au collisions.

The comparison of Λ polarization in Ru+Ru, Zr+Zr, and Au+Au collisions found no system-size dependence [20], consistent with v_1 measurements and constraining vorticity [21]. Global polarization can also probe the residual magnetic field via $\Delta P_H = P_{\bar{\Lambda}} - P_\Lambda = \frac{2|\mu_\Lambda|B}{T}$ [22]. As shown in Fig. 3(b), no significant difference between Λ and $\bar{\Lambda}$ polarizations is observed, indicating the magnetic field has largely vanished by Λ formation.

Multistrange hyperons, such as Ξ (spin 1/2) and Ω (spin 3/2), are produced earlier in the collision and experience longer exposure to the vortical field. Their global polarization in Au+Au collisions at $\sqrt{s_{NN}}$ = 7.7–27 GeV provides insights into the system's hydrodynamic evolution and vorticity. As shown in Fig. 4(a), Ω^- polarization is significant and enhanced over Λ at low energies ($> 2\sigma$), while $\Xi^-(dss)$ polarization (Fig. 4(b)) is consistent with Λ, reflecting expected polarization transfer. Global polarization exhibits a clear collision-energy dependence, with magnitudes varying between Λ, Ξ, and Ω. Measurements use both the direct angular distribution of daughter Λ in the Ξ/Ω rest frame and extraction via spin transfer, with coefficients $C_{\Xi\to\Lambda} \approx 0.944$ and $C_{\Omega\to\Lambda} \approx 1.0$. The spin-3/2 Ω may probe higher-spin dynamics. Polarization increases toward more peripheral collisions but shows no significant dependence on rapidity or transverse momentum.

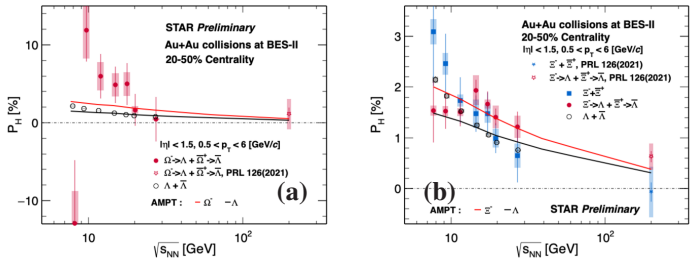

Figure 4. Beam energy dependence of (a) P_H of Ω^- and Ω^+ and (b) Ξ^- and Ξ^+ from direct measurements and from Λ spin transfer in Au+Au collisions.

Longitudinal spin polarization (P_z) probes spin dynamics along the beam direction, providing sensitivity to local vorticity and spin medium coupling. ALICE measured longitudinal polarization of strange hadrons in high-statistics Run 3 Pb+Pb collisions at 5.36 TeV, finding comparable polarization across different harmonics. CMS reported longitudinal hyperon polarization in p+Pb collisions at 8.16 TeV, showing nontrivial dependence on p_T and system

size, which cannot be described by current hydrodynamic models. NA61/SHINE observed significant transverse Λ polarization relative to the production plane in p+p collisions at $\sqrt{s}$ = 17.3 GeV, consistent with previous measurements and theoretical expectations, providing insights into the system-size dependence of spin phenomena.

The spin-spin correlation is measured in pp collision at STAR via $\frac{1}{N}\frac{dN}{d\cos\theta^\star} = \frac{1}{2}[1 + \alpha_1\alpha_2 P_{\Lambda_1\Lambda_2}\cos\theta^\star]$, where $\theta^\star$ is the opening angle between the two boosted (anti-)protons in their respective parent rest frames [23]. Virtual quark–antiquark pairs, particularly strange-quark pairs, can emerge from the vacuum. Figure 5 shows the first evidence of spin correlation between $\Lambda\bar{\Lambda}$ pairs, separating short-range (left) and long-range (right) correlations. A significant short-range correlation is observed ($> 4\sigma$), while widely separated pairs show no correlation, consistent with quantum decoherence. This suggests that virtual quark–antiquark pairs are spin-entangled before hadronization, connecting QCD vacuum entanglement to the polarization of final-state hadrons, and motivates future measurements in AA collisions.

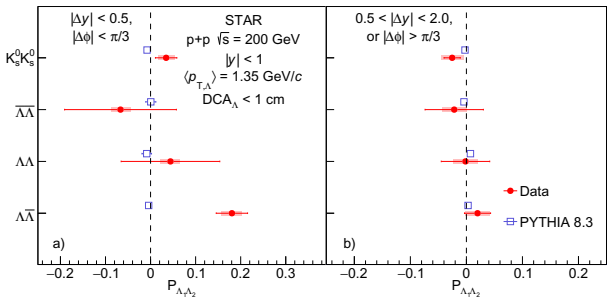

Figure 5. Spin correlation of Λ pairs in (a) short-range and (b) long-range in p+p collision at 200 GeV [23].

4 Spin Alignment

As vector mesons (spin-1) decay through the strong force with parity conservation, a direct measurement of spin polarization is zero. Instead, the variation of spin anisotropy could be quantified by the ρ_{00}, the diagonal component of the spin density matrix [24]. The spin alignment can be measured from emitted particle distribution: $\frac{dN}{d\cos\theta^\star} \propto (1-\rho_{00}) + (3\rho_{00}-1)\cos^2\theta^\star$, where $\theta^\star$ denotes the angle between the decay product along the chosen quantization axis in the vector meson rest frame.

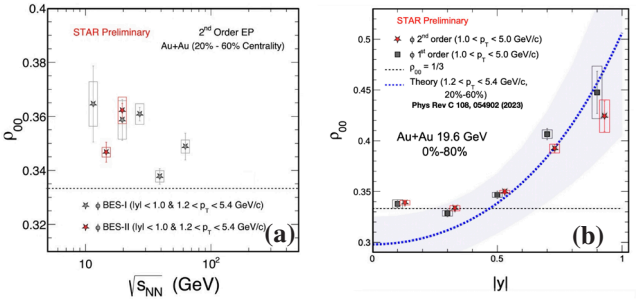

Figure 6. (a) Beam energy dependence of ρ_{00} for ϕ meson in Au+Au. (b) Rapidity dependence of ρ_{00} in Au+Au at $\sqrt{s_{NN}}$ = 19.6 GeV.

The STAR Collaboration reported a significant global spin alignment for ϕ mesons with $\rho_{00} > 1/3$ in Au+Au collisions based on BES-I data in Au+Au collisions at 7.7–200 GeV [25], which cannot be explained by the conventional mechanisms and supports the existence of the ϕ-meson force field. Figure 6 (a) presents the measurements of ϕ-meson global spin alignment using BES-II data in Au+Au collisions at $\sqrt{s_{\rm NN}}$ = 14.6 and 19.6 GeV. The beam energy dependence of ρ_{00} is confirmed with much higher statistical significance, indicating that the spin-0 state is statistically favored. The rapidity dependence of ρ_{00} in Fig. 6 (b) shows an increase with rapidity $|y|$, consistent with predictions from the strong force field

model [26]. No significant difference is observed between results extracted using the first- and second-order event planes. The underlying dynamics of such strong-force fluctuations needs further theoretical investigation.

Figure 7 shows the first measurement of $D^{\star+}$ spin alignment in 30–50% Pb+Pb collisions at $\sqrt{s_{NN}}$ = 5.02 TeV by the ALICE Collaboration [27]. The prompt $D^{\star+}$ mesons are selected with $4 < p_T < 30$ GeV/c in two rapidity intervals, $|y| < 0.3$ and $0.3 < |y| < 0.8$, and compared to inclusive J/Ψ spin alignment at forward rapidity ($2.5 < y < 4$). Evidence for spin alignment $\rho_{00} > 1/3$ is observed for $p_T > 15$ GeV/c and $0.3 < |y| < 0.8$ with a significance of 3σ. In contrast, at lower p_T, the J/Ψ ρ_{00} drops below 1/3, potentially explained by quark coalescence that expects c and $\bar{c}$ to have opposite spin directions. In addition, a larger ρ_{00} is observed at higher rapidity, consistent with the trend previously reported at RHIC. The $D^{\star+}$ mesons are produced early and are potentially sensitive to the magnetic field. This finding indicates that the c quark fragmentation could be polarized by the magnetic field. In p+p collisions, no spin alignment is seen for prompt $D^{\star+}$ mesons, providing a baseline for the Pb+Pb results, whereas non-prompt $D^{\star+}$ mesons exhibit large ρ_{00} in the helicity frame and values below 1/3 in the production frame, consistent with helicity conservation during anisotropic expansion of the parent bottom hadron. These findings impose new constraints on charmonium production dynamics and the magnetic field strength in heavy-ion collisions.

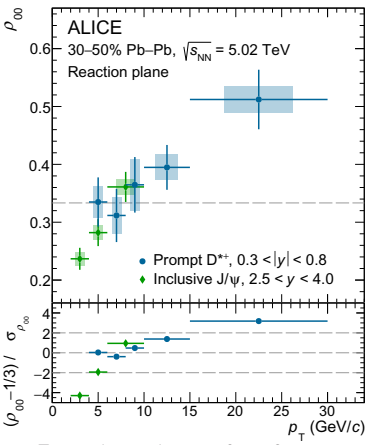

Figure 7. p_T dependence of ρ_{00} for prompt $D^{\star+}$ and inclusive J/ψ in 30–50% Pb+Pb collisions at $\sqrt{s_{NN}}$ = 5.02 GeV (top) and its deviation from 1/3 (bottom) [27].

Lastly, it is worth mentioning recent progress in exploring the inter-correlation between the CME and spin alignment, as both observables are sensitive to two-particle emission patterns across the reaction plane from resonance decays and may influence each other. In addition to the established correlation between ρ_{00} and $\Delta\gamma^{112}$ [11], a recent study shows that the off-diagonal spin density matrix element ρ_{1-1} also impacts $\Delta\gamma^{112}$, but in the opposite direction [28]. Figure 8 shows the contributions from the spin density matrix elements evaluated using a multi-phase transport model (AMPT) and a toy model for Au+Au collisions at $\sqrt{s_{NN}}$ = 200 GeV. The real part $Re\{\rho_{1-1}\}$ reduces CME observables linearly, contrary to the effect of ρ_{00}, while the remaining elements show negligible influence. Since ρ_{1-1} reflects spin coherence and could be nonzero in heavy-ion collisions due to local spin polarization or spin–spin correlations, both $Re\{\rho_{1-1}\}$ and ρ_{00} may play an important role in interpreting the CME-related measurements. This background is also found to vanish when v_2 is constrained to zero, as illustrated in Fig. 8(b).

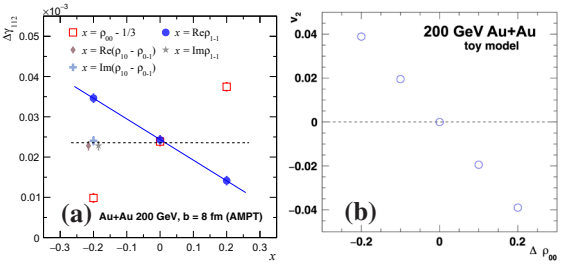

Figure 8. (a) $\Delta\gamma_{112}$ vs various elements of the ρ spin density matrix in Au+Au at 200 GeV from the AMPT model [28]; (b) v_2 vs ρ_{00}, deviating from 1/3 in a toy model.

5 Summary

We review recent highlights in relativistic nuclear collisions on three QCD phenomena: the chiral effect, spin polarization, and global spin alignment. The CME and CMW addresses an intrinsic property of QCD, and the new STAR CME results report a residual charge separation around 3σ at three beam energies between 10 and 20 GeV. Global polarization measurements reveal substantial vorticity of the QGP, with no system dependence observed for Λ polarization. A potential enhancement in Ω^- global polarization over Λ and Ξ is reported at lower RHIC energies. Longitudial polarization provides insight into the collision system size and supports further theoretical development. The observation of spin-spin correlations between short-range Λ-$\bar{\Lambda}$ pairs in p+p collisions offers a new avenue to explore quark confinement and spin quantum entanglement. Global spin alignment probes strong force field fluctuations, with dependence on beam energy and rapidity, indicating sensitivity to the vector-meson strong force field. The observed p_T dependence of ρ_{00} for J/Ψ and D^{*+} further constrains the charmonium production mechanisms and the magnetic field strength. Recent studies suggest that these observables may be interrelated, as spin alignment can serve as a background to the CME measurements, and vice versa.

References

[1] Z. Liang and X. Wang, Phys. Rev. Lett. **94**, 102301 (2005)
[2] V. Skokov, A. Illarionov, and V. Toneev, Int. J. Mod. Phys. A **24**, 5925 (2009).
[3] D. E. Kharzeev, L. D. McLerran, and H. J. Warringa, Nucl. Phys. A **803**, 227 (2008).
[4] D. E. Kharzeev, H. Yee, Phys. Rev. D **83**, 085007 (2011).
[5] S. A. Voloshin, Phys. Rev. C **70**, 057901 (2004).
[6] N. Magdy *et al.*Phys. Rev. C **97**, 061901 (2018).
[7] A. H. Tang, Chin. Phys. C **44**, 054101 (2020).
[8] [STAR Collaboration] Phys. Rev. C **105**, 014901 (2022)
[9] A. M. Sirunyan *et al.* [CMS Collaboration], Phys. Rev. C **97**, 044912 (2018).
[10] S. Acharya *et al.* [ALICE Collaboration], J. High Energy Phys. **09**, 160 (2020).
[11] Z. Xu, B. Chan, G. Wang, A. Tang, H. Huang, Phys. Lett. B **848**, 138367 (2024).
[12] [STAR Collaboration], arXiv:2506.00275 [nucl-ex] (2025).
[13] [STAR Collaboration], arXiv:2506.00278 [nucl-ex] (2025).
[14] Z. Xu, G. Wang, A. H. Tang, H. Z. Huang, Phys. Rev. C **107**, L061902 (2023).
[15] L. Adamczyk *et al.* [STAR Collaboration], Phys. Rev. Lett. **113**, 052302 (2014).
[16] B. I. Abelev *et al.* [STAR Collaboration] Phys. Rev. C **76**, 024915 (2007)
[17] L. Adamczyk *et al.* [STAR Collaboration], Nature **548** (2017) 62–65.
[18] M. S. Abdallah *et al.* [STAR Collaboration], Phys. Rev. C **104** (2021) 61901.
[19] R. Yassine et al. [HADES Collaboration], Phys. Lett. B, **835** (2022) 137506
[20] [STAR Collaboration], arXiv:2505.05046 [nucl-ex] (2025).
[21] G. Agakishiev *et al.* [STAR Collaboration], Phys. Rev. C **85**, 014901 (2012)
[22] F. Becattini *et al.*Phys. Rev. C **95**, 054902 (2017)
[23] [STAR Collaboration], arXiv:2506.05499 [nucl-ex] (2025).
[24] B. I. Abelev *et al.* [STAR Collaboration], Phys. Rev. C **77**, 061902(R) (2008)
[25] M. S. Abdallah *et al.* [STAR Collaboration], Nature **614** (2023) 244–248
[26] Sheng et al., Phys. Rev. C **108**, 054902 (2023)
[27] [ALICE Collaboration] arXiv:2504.00714 [nucl-ex] (2025).
[28] Z. Wang et al., Phys. Rev. C **111** 014910 (2025)